RESEARCH ARTICLE

NANO · MICRO small
www.small-journal.com

Unleashing the Power of Sn_2S_3 Quantum Dots: Advancing Ultrafast and Ultrastable Sodium/Potassium-Ion Batteries with N, S Co-Doped Carbon Fiber Network

*Hui Wu, Shuang Li, and Xuebin Yu**

Tin sulfide (Sn_2S_3) has been recognized as a potential anode material for sodium-ion batteries (SIBs) and potassium-ion batteries (PIBs) due to its high theoretical capacities. However, the sluggish ion diffusion kinetics, low conductivity, and severe volume changes during cycling have limited its practical application. In this study, Sn_2S_3 quantum dots (QDs) (≈1.6 nm) homogeneously embedded in an N, S co-doped carbon fiber network (Sn_2S_3-CFN) are successfully fabricated by sequential freeze-drying, carbonization, and sulfidation strategies. As anode materials, the Sn_2S_3-CFN delivers high reversible capacities and excellent rate capability (300.0 mAh g^{-1} at 10 A g^{-1} and 250.0 mAh g^{-1} at 20 A g^{-1} for SIBs; 165.3 mAh g^{-1} at 5 A g^{-1} and 100.0 mAh g^{-1} at 10 A g^{-1} for PIBs) and superior long-life cycling capability (279.6 mAh g^{-1} after 10 000 cycles at 5 A g^{-1} for SIBs; 166.3 mAh g^{-1} after 5 000 cycles at 2 A g^{-1} for PIBs). According to experimental analysis and theoretical calculations, the exceptional performance of the Sn_2S_3-CFN composite can be attributed to the synergistic effect of the conductive carbon fiber network and the Sn_2S_3 quantum dots, which contribute to the structural stability, reversible electrochemical reactions, and superior electron transportation and ions diffusion.

1. Introduction

The escalating global demand for energy, coupled with growing concerns about environmental degradation due to fossil fuel consumption, has fueled a pressing need for advanced electrical energy storage systems in recent decades.[1] In response to these challenges, lithium-ion batteries (LIBs) have gained widespread adoption in energy storage applications.[2] However, the inherent limitations arising from the scarcity and uneven distribution of lithium resources pose a significant barrier to the large-scale application of LIBs.[3] This has spurred an exploration of alternative rechargeable battery systems, with sodium-ion batteries (SIBs) and potassium-ion batteries (PIBs) emerging as promising candidates due to their abundance and cost-effectiveness. Despite their potential, SIBs and PIBs face challenges related to significant electrode volume variation and sluggish reaction kinetics, attributed to the larger cation radius of Na^+ and K^+ compared to Li^+. This results in lower capacity and poor cyclic stability, hindering practical applications. To address these challenges, extensive research has been conducted on various anode materials, including carbonaceous materials, alloys, and metal oxides/sulfides.[4]

Among metal sulfides, Sn-based sulfides compounds, such as SnS, SnS_2, and Sn_2S_3, stand out as promising anode materials for SIBs and PIBs, owing to their unique layered structures and high theoretical capacity (e.g., 1022 mAh g^{-1} for SnS and 1136 mAh g^{-1} for SnS_2).[5] In comparison to the widely studied SnS and SnS_2 electrode materials, Sn_2S_3 not only has an intrinsically higher theoretical capacity (1189 mAh g^{-1}) but also possesses higher electrical conductivity (4.35×10^{-3} S cm^{-1}), representing its great potential as a promising anode candidate for both SIBs and PIBs.[5] Additionally, DFT calculations have verified that the diffusion energy barrier of Na^+ transition in Sn_2S_3 was lowest, compared with that of SnS and SnS_2, and the Sn—S bonds could be rebuilt during the discharge/charge process.[6] However, there have been few reports on the application of Sn_2S_3 electrodes in SIBs so far. The paucity of research on the utilization of Sn_2S_3 electrodes in SIBs and PIBs may be ascribed to the significant volumetric changes and incomplete $Na_{15}Sn_4$ alloy formation during the repetitive discharge processes.[7] These drawbacks result in significant degradation of the electrochemical performance, manifesting as poor rate capability, rapid capacity fading, and inferior reversible capacity that falls substantially short of the theoretical capacity.[7] To overcome these issues, several approaches such as nanosizing, hollow microparticle design, integration with Ti_3C_2 sheets, and heterostructure construction have been proposed by different research groups,[6–8] and the electrochemical performance of Sn_2S_3 in SIBs has been improved to a certain extent. However, the electrochemical performance of Sn_2S_3 still lags behind other tin sulfide anodes, i.e.,

H. Wu, S. Li, X. Yu
Department of Materials Science
Fudan University
Shanghai 200433, China
E-mail: yuxuebin@fudan.edu.cn
S. Li
Wanxiang A123 Systems Corporation
Hangzhou 311215, China

The ORCID identification number(s) for the author(s) of this article can be found under https://doi.org/10.1002/smll.202311196

DOI: 10.1002/smll.202311196

SnS,[9] SnS_2.[10] These suboptimal electrochemical performances of modified Sn_2S_3 anodes may be ascribed to unresolved issues, such as the evitable pulverization problems induced by the conversion and alloying reaction, insufficient conductivity of the modified composite, and incomplete Na—Sn alloying reaction. Recent reports suggest that downsizing metal sulfides to quantum dots (QDs) with diameters below 10 nm can overcome kinetic and thermodynamic constraints, enhancing electrochemical reactions and achieving higher specific capacity.[11] The integration of Sn_2S_3 QDs into a well-designed carbon matrix, with heteroatom doping, has been proposed to mitigate side effects such as increased solid-electrolyte interphase (SEI) layer and particle aggregation.[12] However, the design of Sn_2S_3 QDs composited with a heteroatom-doped carbon matrix remains a formidable challenge.

Herein, we identified an opportunity to develop an advanced Sn_2S_3-based anode by integrating the Sn_2S_3 QDs and the N, S co-doped carbon fiber network structure to significantly enhance the electrochemical performance of Sn_2S_3. Apart from the aforementioned merits of carbon matrix, the introduction of a carbon fiber network structure with heteroatom doping could not only offer abundant ion/electron transport channels but also generate internal void space between fibers to buffer the volume variation, which plays a key role in further improving the whole electrochemical performance of Sn_2S_3. In this work, Sn_2S_3 QDs (≈1.6 nm) embedded in an N, S co-doped carbon fiber network (Sn_2S_3-CFN) were synthesized by sequential freeze-drying, carbonization, and sulfidation strategies. During the synthesis process, the chitosan fibrous 3D network structures were formed during the freeze-drying process and were used as the precursor of the carbon framework, which could effectively limit the aggregation and growth of the Sn_2S_3 QDs during high-temperature treatment. The Sn_2S_3 QDs can remarkably decrease the ion diffusion length, effectively buffer the volume expansion, and help overcome the kinetic and thermodynamic barriers of electrochemical reactions. The N, S co-doped carbon fiber network in Sn_2S_3-CFN serves as a conductive framework, provides 3D paths for ion/electron delivery, and maintains structural stability. The existence of N, S co-doped carbon modification can effectively hamper the aggregation and growth of Sn_2S_3 QDs, and significantly reduce both the adsorbed energies and diffusion energy barriers of Na/K atom in the interlayer of Sn_2S_3-CFN, enhancing the reactivity for sodium/potassium storage. Benefiting from the synergistic interactions between Sn_2S_3 QDs and N, S co-doped carbon fibers network, the as-prepared Sn_2S_3-CFN exhibits significantly enhanced rate capability and cyclic stability as an anode material for SIBs and PIBs. When used as the anode material for SIBs, it exhibited excellent electrochemical performance, evidenced by the ultralong cycle life of up to 10 000 cycles (279.6 mAh g^{-1}) at 5 A g^{-1} and the excellent rate capability of 300.0 and 250.0 mAh g^{-1} at high current densities of 10 and 20 A g^{-1}, respectively. Moreover, Sn_2S_3-CFN-2 delivered an impressive electrochemical performance in PIBs, demonstrated by the long-term cycling stability of more than 5000 cycles with a high specific capacity of 166.3 mAh g^{-1} at 2 A g^{-1} and the excellent rate capability of up to 100 mAh g^{-1} at a current density of 10 A g^{-1}. This work provides meaningful insights into the development of advanced electrode materials for electrochemical energy storage.

2. Results and Discussion

Figure 1a shows a typical preparation process of Sn_2S_3-CFN composites. Initially, an $SnCl_2$ solution was incrementally added to the chitosan solution with continuous stirring to achieve a homogenous mixture, which was then freeze-dried. The resulting product was a chitosan fiber composite material with a uniform distribution of Sn^{2+} ions throughout the mixed powder.[13] The Sn_2S_3 QDs embedded in the N, S co-doped carbon nanofiber network were obtained by carbonizing freezing-dried samples, followed by the sulfidation under an Ar atmosphere. The microstructure and morphology of the as-prepared Sn_2S_3-CFN composites were investigated by field-emission scanning electron microscopy (FESEM), transmission electron microscopy (TEM), high-resolution TEM (HRTEM), and scanning transmission electron microscopy (STEM). Figure 1b,e shows the FESEM images of Sn_2S_3-CFN-1, in which the composite showed carbon nanofibers with some irregular segments formed and attached to the surface of carbon fibers. Smooth carbon fibers without any associated particles were obtained by increasing the chitosan quantity to 0.33 g, as displayed in Figure 1c,f. The fibers in the Sn_2S_3-CFN-2 composite have a uniform diameter of approximately 100 nm and form an interconnected fiber network architecture. As the chitosan quantity was increased to 0.66 g, no carbon nanofibers were observed in the final composite, as illustrated in Figure 1d,g, in which the Sn_2S_3-CFN-3 composite is highly irregular in shape and size. Additionally, the bulk Sn_2S_3 sample also presents an irregular morphology with large size distribution over a range of 10 µm, as shown in Figure S1, Supporting Information. Moreover, the more detailed microscopic structure of the Sn_2S_3-CFN-2 composite was investigated by the TEM and HRTEM (Figure 1h–j), revealing that Sn_2S_3 QDs were uniformly and tightly embedded in the carbon fiber, with average diameters of ≈1.6 nm. Moreover, Figure 1j shows the clear lattice fringes with a d-spacing of ≈0.335 nm, which are consistent with the (111) crystal face of Sn_2S_3. The STEM energy-dispersive spectroscopy (EDS) mapping images suggest that the C, Sn, S, and N elements of the Sn_2S_3-CFN-2 composite are uniformly distributed in the carbon framework (Figure 1k).

As depicted in **Figure 2a**, the XRD patterns revealed that the diffraction peaks of the Sn_2S_3-CFN-2/3 composites were consistent with the orthorhombic Sn_2S_3 having the *Pnam* space group (JCPDS Card No. 72-0031), indicating their high purity with no detectable impurity peaks. The Sn_2S_3-CFN-1 composite displayed a small peak at 15.1°, attributable to the formation of SnS_2, implying a different composition or impurities in this composite.[14] Furthermore, the XRD pattern of the commercial Sn_2S_3 sample was also obtained and is presented in Figure S2, Supporting Information. This additional analysis provides a basis for comparison and confirms the structural similarity of the synthesized Sn_2S_3-CFN composites to the commercial Sn_2S_3 sample. The Raman spectrum of the Sn_2S_3-CFN composite was presented in Figure 2b revealing two significant peaks at around 1360 and 1580 cm^{-1}, corresponding to the D-bands and G-bands of carbon materials, respectively.[15] The intensity ratios of D/G-bands (I_D/I_G) for Sn_2S_3-CFN-1, Sn_2S_3-CFN-2, and Sn_2S_3-CFN-3 composites were calculated as 0.94, 0.97, and 0.93, respectively. Typically, the I_D/I_G values reflect the disordered structure and defect density of carbon materials, where higher values indicate

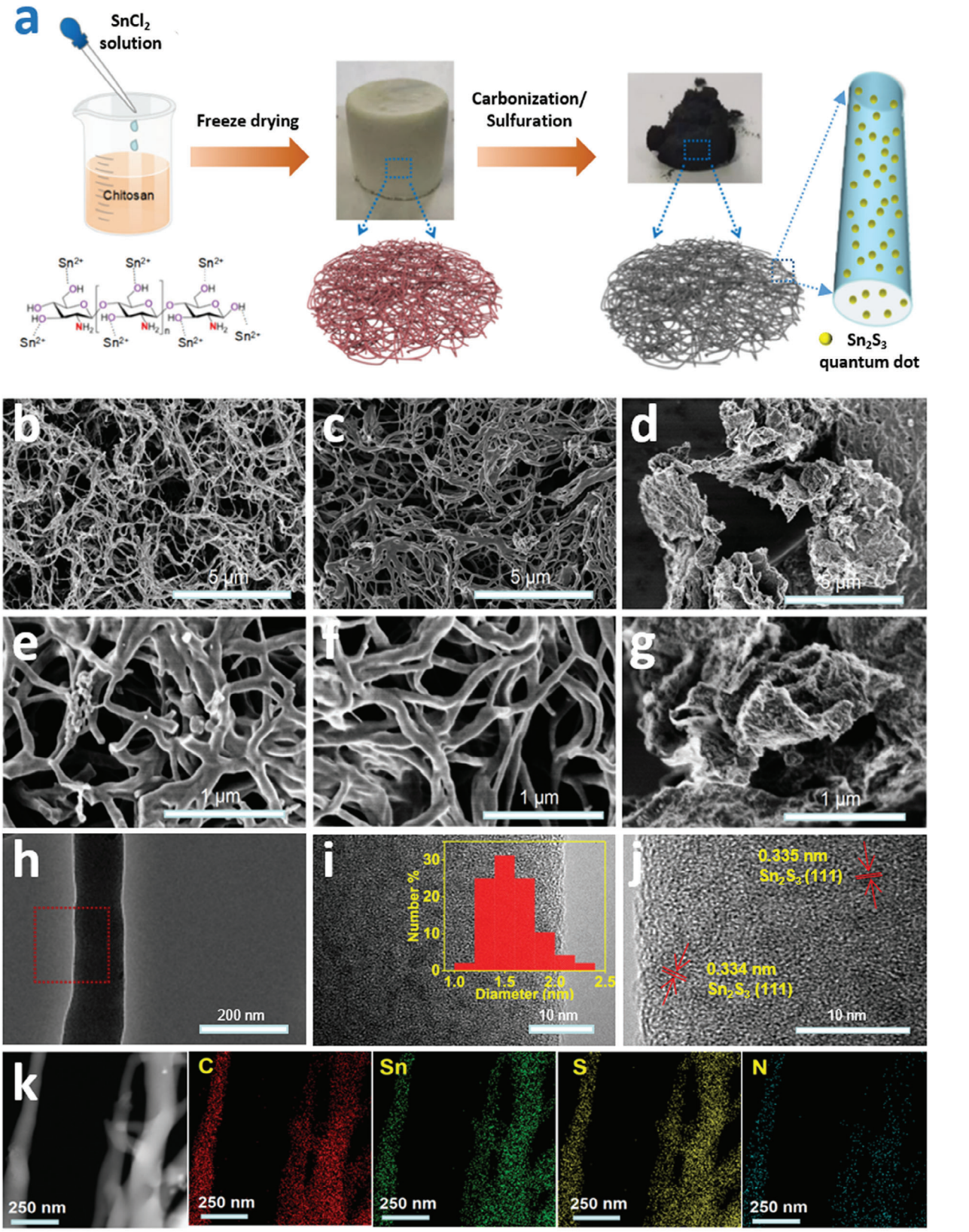

Figure 1. a) Schematic illustration of the synthesis process of Sn_2S_3-CFN composites. SEM images of b,e) Sn_2S_3-CFN-1, c,f) Sn_2S_3-CFN-2, and d,g) Sn_2S_3-CFN-3 composites. h,i) TEM, j) HRTEM, and k) STEM-EDS mapping images of Sn_2S_3-CFN-2 composite, and size distribution is inserted in panel i.

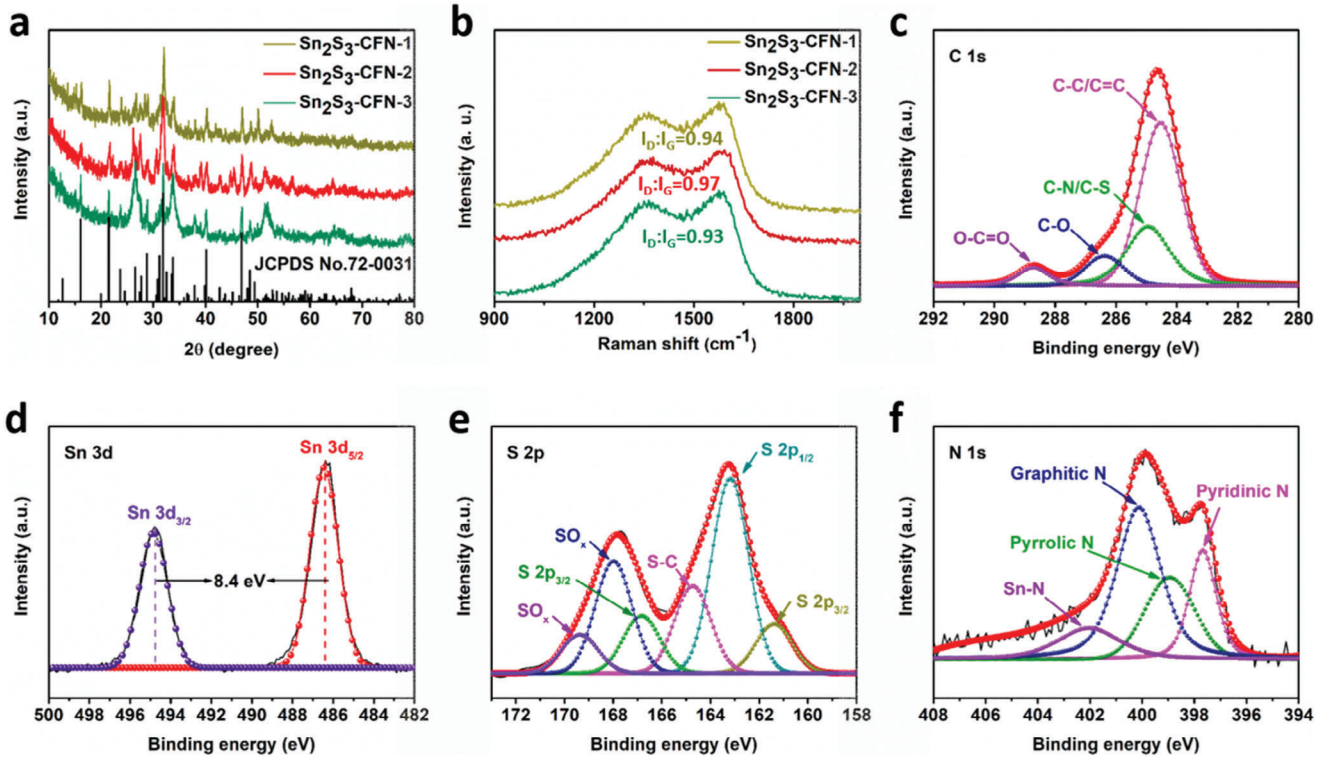

Figure 2. a) XRD patterns and b) Raman spectra of the as-prepared Sn_2S_3-CFN composites. c) C 1s, d) Sn 3d, e) S 2p, and f) N 1s XPS spectra of Sn_2S_3-CFN-2 composite.

more disordered structures and defects. The change in the I_D/I_G ratio observed in the Raman spectra from Sn_2S_3-CFN-1 to Sn_2S_3-CFN-3 indicates variations in the structural and compositional properties of the samples. Changes in precursor ratios of Sn and chitosan might play a crucial role in leading to variations in the arrangement of carbon atoms and the development of defects, influencing the Raman spectra. These results provide insights into the structural properties of the Sn_2S_3-CFN composites and highlight the potential of these materials for various applications.[16] To gain further insight into the composition of the Sn_2S_3-CFN-2 composite, an XPS analysis was conducted. XPS survey spectrum shows that the as-prepared Sn_2S_3-CFN-2 composite mainly contains C, Sn, S, and N elements (Figure S3, Supporting Information). The high-resolution C 1s spectrum (Figure 2c) revealed that the peaks of the C 1s can be deconvoluted into four component peaks. The main peak observed at 284.5 eV can be attributed to C—C/C═C, while the other three minor peaks located at 288.7, 286.4 eV, and 285.0 eV, were assigned to the O═C—O bond, C—O bond, and C—N/C—S bond, respectively.[17] The high-resolution Sn 3d spectrum presented in Figure 2d showed the binding energies of Sn $3d_{5/2}$ and Sn $3d_{3/2}$ at approximately 486.38 and 494.78 eV, respectively. The observed difference in the binding energy between the two Sn oxidation states was 8.4 eV, which is consistent with the reference values reported by Avellaneda et al.[18] Figure 2e shows the high-resolution S 2p spectrum. The two peaks at around 161.38 and 166.78 eV can be assigned to S $2p_{3/2}$ of S^{2-}, and another peak located at 163.18 eV is consistent with the S $2p_{1/2}$ of S^{2-}.[19] The peak observed at 164.68 eV was attributed to the S—C bond.[20] Two additional peaks at 168.0 and 169.38 eV were also observed, which could be attributed to the partial surface oxidation of the samples and the formation of SO_x.[21] Furthermore, the high-resolution N1s spectrum in Figure 2f can be convoluted in graphitic N (399.0 eV), pyrrolic N (400.2 eV), pyridinic N (397.68 eV), and Sn—N (402 eV).[19a] The self-doped nitrogen species in the Sn_2S_3-CFN-2 composite contribute a significant number of electrons to the π-conjugated system of carbon, which can enhance the electronic conductivity of the material.[22] Moreover, the presence of pyrrolic and pyridinic nitrogen species can introduce defects in carbon and create active sites for the storage of Na^+ and K^+ ions. Moreover, in order to obtain the weight percentage of Sn_2S_3 in Sn_2S_3-CFN-2, thermogravimetric analysis (TGA) was carried out with samples in Air flow, and the resulting profile was presented in Figure S4, Supporting Information. The initial weight loss (≈0.3%) was attributed to the evaporation of the absorbed water. The weight ratio of 24.8% can be attributed to carbon and the oxidation of Sn_2S_3. Therefore, the ratio of carbon and Sn_2S_3 in the composite was calculated to be 83.2% and 16.8%, respectively.

To evaluate the Na^+ storage behavior of the as-synthesized Sn_2S_3-CFN composites and bulk Sn_2S_3 sample, their electrochemical performances were evaluated through CV and galvanostatic discharge-charge (GDC) in half-cell configurations by assembling CR2032-type coin cells. The CV curves of the Sn_2S_3-CFN-2 electrodes for the first three cycles were measured from 0.01 and 3 V with a slow scan rate of 0.1 mV s^{-1} (**Figure 3a**). In the initial cathodic sweep, there is a small reductive peak at 1.05 V which could be attributed to the insertion of Na^+ with the formation of $Na_xSn_2S_3$ ($xNa + Sn_2S_3 \rightarrow Na_xSn_2S_3$).[8a]

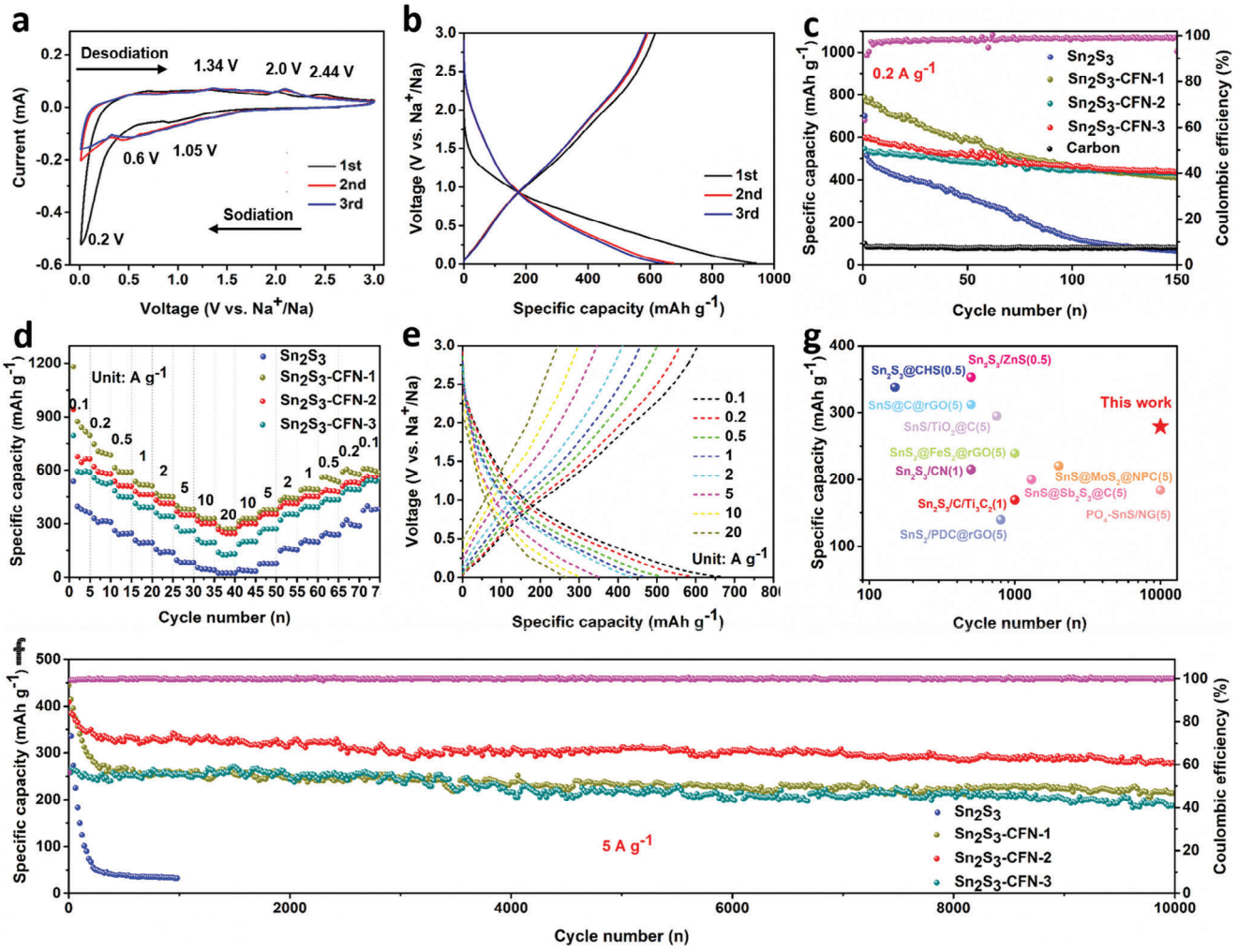

Figure 3. Electrochemical sodium storage performances of Sn_2S_3/C composites and pure Sn_2S_3 anodes. a) CV curves of Sn_2S_3-CFN-2 at a scan rate of 0.1 mV s^{-1} in a potential range of 0.01–3.0 V. b) GDC profiles of Sn_2S_3-CFN-2 at a current density of 0.1 A g^{-1}. c) Cycling performance of Sn_2S_3-CFN, bulk Sn_2S_3 and carbon electrodes at a current density of 0.2 A g^{-1}. d) Rate performance of Sn_2S_3-CFN and bulk Sn_2S_3 electrodes with current densities ranging from 0.1 to 20 A g^{-1}. e) Charge and discharge profiles at current densities ranging from 0.1 to 20 A g^{-1}. f) Cycling performance of Sn_2S_3-CFN and bulk Sn_2S_3 electrodes at a current density of 5 A g^{-1}. g) Comparison of cycling performance between Sn_2S_3-CFN-2 and all previously reported Sn_2S_3-based anodes and other representative Sn-S-based anodes for SIBs.

Additionally, a broad peak below 0.6 V may correspond to the irreversible electrolyte decomposition, formation of the SEI layer, and the reaction between the Na^+ and Sn_2S_3 accompanied by the generation of sodium-rich Na_ySn phase and sodium sulfide (Na_2S) with $((6+2y-x)Na + Na_xSn_2S_3 \rightarrow 3Na_2S + 2Na_ySn)$.[6] In the following anodic sweep, the reversible process occurred, and several minor peaks located at 1.34, 2.00, and 2.44 V, were observed as a result of the multistep desodiation process ($3Na_2S + 2Na_ySn \rightarrow Sn_2S_3 + (6+2y)$ Na). In subsequent cycles, the minor peaks shift to a higher potential, which may be attributable to the reduced electrode polarization after the initial activation of the Sn_2S_3-CFN-2 electrode. Figure 3b displays the first three GDC profiles of the Sn_2S_3-CFN-2 electrode at a low current density of 100 mA g^{-1} while no obvious plateaus were observed. Besides, the first discharge and charge profiles of the Sn_2S_3-CFN-2 electrode exhibited capacities of 941 and 616 mAh g^{-1}, respectively, resulting in an initial Coulombic efficiency (ICE) of up to 65.4%. This initial capacity loss was mainly due to the formation of SEI film on the electrode. which were commonly observed in the nanostructured anodes for SIBs. Figure 3c compares the cyclic performances of Sn_2S_3-CFN composites and bulk Sn_2S_3 at a current density of 0.2 A g^{-1}. It can be seen that Sn_2S_3-CFN electrodes exhibit better cycling stability than bulk Sn_2S_3 electrodes. As for bulk Sn_2S_3, it suffers from severe capacity fading, which delivers a low reversible capacity of 66.8 mAh g^{-1} after 100 cycles. Besides, noted that among the Sn_2S_3-CFN composites, the Sn_2S_3-CFN-2 electrode achieves the most appreciable capacity and cycling stability. After 100 cycles, the Sn_2S_3-CFN-2 electrode delivers a high reversible capacity of 462.1 mAh g^{-1}, which is higher than that of Sn_2S_3-CFN-1 electrode (461 mAh g^{-1}) and Sn_2S_3-CFN-3 electrode (443 mAh g^{-1}).

Furthermore, benefiting from the synergistic effect of Sn_2S_3 QDs and N, S co-doped carbon framework, the Sn_2S_3-CFN composites demonstrated better rate capability than that of bulk

Sn_2S_3 electrodes (Figure 3d). Especially for the Sn_2S_3-CFN-2 composite, the high reversible capacity of 676.0, 591.6, 513.1, 464.3, 415.2, 348.7, and 300.0 mAh g^{-1} can be achieved at current densities of 0.1, 0.2, 0.5, 1.0, 2.0, 5.0, and 10 A g^{-1}, respectively. It is noteworthy that even at an extremely high specific current of 20 A g^{-1}, a capacity of 250.0 mAh g^{-1} is still achieved. In comparison, other prepared electrodes delivered inferior rate capability, as listed in Table S1, Supporting Information. the Sn_2S_3-CFN-3 electrode exhibited a fast capacity fade, which could be mainly ascribed to the existence of segments attached to the 3D CFN framework. The inferior capacity retention of the Sn_2S_3-CFN-3 electrode can be attributed to the absence of a well-designed carbon fiber network architecture. In contrast, bulk Sn_2S_3 without modification showed poor rate capability. The GDC voltage profiles of Sn_2S_3-CFN-2 at various current densities ranging from 0.1 to 20 A g^{-1} are presented in Figure 3e. The GDC profiles of Sn_2S_3-CFN-2 remain stable upon gradually increasing the current density. To evaluate the long-term and high-rate cycling stability, the Sn_2S_3-CFN composites and pure Sn_2S_3 were further evaluated by GDC measurement at a larger current density of 5.0 A g^{-1}, as shown in Figure 3f. It can be seen that the Sn_2S_3-CFN composites all exhibited excellent cycling stability, while bulk Sn_2S_3 material suffered from serious capacity fade. Impressively, after 10 000 cycles, the Sn_2S_3-CFN-2 electrode shows a high reversible capacity of 279 mAh g^{-1}, which is higher than that of the Sn_2S_3-CFN-1 electrode (212 mAh g^{-1}) and Sn_2S_3-CFN-3 electrode (187 mAh g^{-1}). These results further demonstrate the high sodium-ion storage capability and superior cycling stability of Sn_2S_3-CFN-2 composites. As for bulk Sn_2S_3, it suffers from severe capacity fading, which delivers a low reversible capacity of 31.9 mAh g^{-1} after 1000 cycles. Moreover, to clarify the relationship between the structure and electrochemical performance, the morphology of the Sn_2S_3-CFN-2 upon cycling was examined. As shown in Figures S5 and S6, Supporting Information, it can be seen that the 3D CFN framework structure of Sn_2S_3-CFN-2 is well maintained after testing at 5 A g^{-1} for 300 cycles. While the pure Sn_2S_3 particles without carbon modification suffered from serious pulverization and aggregation after 300 cycles at 5.0 A g^{-1} (Figure S7, Supporting Information). This result demonstrates that the unique structure efficiently suppresses the particle pulverization and aggregation of Sn_2S_3, thus keeping the structural integrity and stability of the whole electrode and ensuring long-term cycling stability.[23] Additionally, a comparison of the cycling performance of the Sn_2S_3-NFC-2 and all previously reported Sn_2S_3-based anodes and other representative Sn-S-based anodes for SIBs were summarized (Figure 3g).[6–9,24] In contrast to the inferior capacity and cyclability at moderate current densities delivered in representative sodium ion storage, the Sn_2S_3-NFC-2 exhibited remarkable cyclability and capacity, which can be attributed to the optimized structure achieved by the integration of Sn_2S_3 QDs and N, S co-doped carbon framework.

In addition, our results showed that the Sn_2S_3-CFN composite can also be utilized as an anode material for PIBs. To explore the potassium storage properties of the Sn_2S_3-CFN electrodes, various measurements including CV, GDC, rate capability, and cycling stability were performed by constructing half-cells with metallic potassium used as counter electrodes. **Figure** 4a shows the CV curves of the Sn_2S_3-CFN-2 electrode for the first three cycles measured at 0.1 mV s^{-1} within 0.01–3 V, suggesting a storage mechanism analogous to SIBs. During the first discharge process, a small peak at 1.6 V could be attributed to the initial intercalation of K^+ into Sn_2S_3 with the formation of $K_xSn_2S_3$ ($xK + Sn_2S_3 \rightarrow K_xSn_2S_3$). Moreover, the pronounced peak below 1.1 V was generally ascribed to the formation of SEI film and the occurrence of conversion and alloying reactions ($(6+2y-x)\ K + K_xSn_2S_3 \rightarrow 3K_2S + 2K_ySn$), and the intercalation of K ion into the amorphous carbon layer ($xK^+ + C + xe^- \rightarrow K_xC$). In the following anodic sweep, the reversible process occurs, and a small peak located at ≈0.6 V is related to the deintercalation of K ion from amorphous carbon. Moreover, two minor peaks located at 1.02 and 2.35 V were observed, due to the multistep depotassiation process of K—S compounds to Sn_2S_3.[8a] In addition, the shapes of the 2nd and 3rd CV plots were nearly coincident, indicating superior reversibility and cycling stability. Figure 4b presents the GDC profiles of the Sn_2S_3-CFN-2 electrode at a current density of 100 mA g^{-1}. Notably, the profiles for the 2nd and 3rd cycles almost overlap, indicating excellent cycle stability, which is consistent with the CV measurements. The cycling performance of the Sn_2S_3-CFN-2 and bulk Sn_2S_3 electrodes was studied at a low current density of 0.2 A g^{-1}. Figure 4c reveals the outstanding cyclic performance of the Sn_2S_3-CFN-2 electrode. Compared to bulk Sn_2S_3, the Sn_2S_3-CFN-2 electrode achieves a high discharge capacity of 361.8 mAh g^{-1} after 50 cycles, indicating the good electrochemical reversibility of the electrode. While bulk Sn_2S_3 suffers from severe capacity fading, which only delivers a low reversible capacity of 93.0 mAh g^{-1} after 50 cycles. Figure 4d displays the rate performance of the Sn_2S_3-CFN-2 and bulk Sn_2S_3 electrodes, in which the current density was increased stepwise from 0.1 to 10 A g^{-1} and returned to 0.1 A g^{-1}. The Sn_2S_3-CFN-2 electrode delivers the discharge capacities of 539.3, 388.3, 329.3, 292.8, 236.1, and 165.3 mAh g^{-1} under current densities of 0.1, 0.2, 0.5, 1, 2, and, 5 A g^{-1}, respectively. It is noteworthy that even at an extremely high specific current of 10 A g^{-1}, a capacity of 100.0 mAh g^{-1} is still achieved. Notably, the capacity can be almost fully recovered as the current density gradually returns to 0.1 A g^{-1} and the Coulombic efficiency is close to 100%, indicating superior electrochemical reversibility. In comparison, the bulk Sn_2S_3 electrode exhibited a fast capacity fade, which delivers the discharge capacities of 322.8, 198.3, 120.4, 86.11, 66.1, 44.4, and 36.1mAh g^{-1} under current densities of 0.1, 0.2, 0.5, 1, 2, 5, and 10 A g^{-1}, respectively. Moreover, the GDC voltage profiles of Sn_2S_3-CFN-2 at various current densities from 0.1 to 10 A g^{-1} were presented in Figure 4e. It can be seen that the GDC profiles of Sn_2S_3-CFN-2 remain stable with gradually increasing current density. The Sn_2S_3-CFN-2 displayed an initial discharge capacity of 853.3 mAh g^{-1} and an initial charge capacity of 489.6 mAh g^{-1}, resulting in an ICE of up to 57.3%.

Inspired by the excellent rate capability, Sn_2S_3-CFN-2 was also expected to exhibit excellent long-term cycle stability at higher current densities. Thus, the long-term cycling performance of Sn_2S_3-CFN-2 and bulk Sn_2S_3 electrodes at a high current density of 2 A g^{-1} was investigated, as recorded in Figure 4f. It can be seen that the bulk Sn_2S_3 electrode suffers from severe capacity fading during cycling at 2 A g^{-1}. While for the Sn_2S_3-CFN-2 electrode, it exhibits an ultrastable cycling behavior at the same current density, which maintained capacities of 184.3, 186.2, 197.7, 173.7, and 166.3 mAh g^{-1} after 1000, 2000, 3000, 4000, and 5 000 cycles. The average capacity fading was only

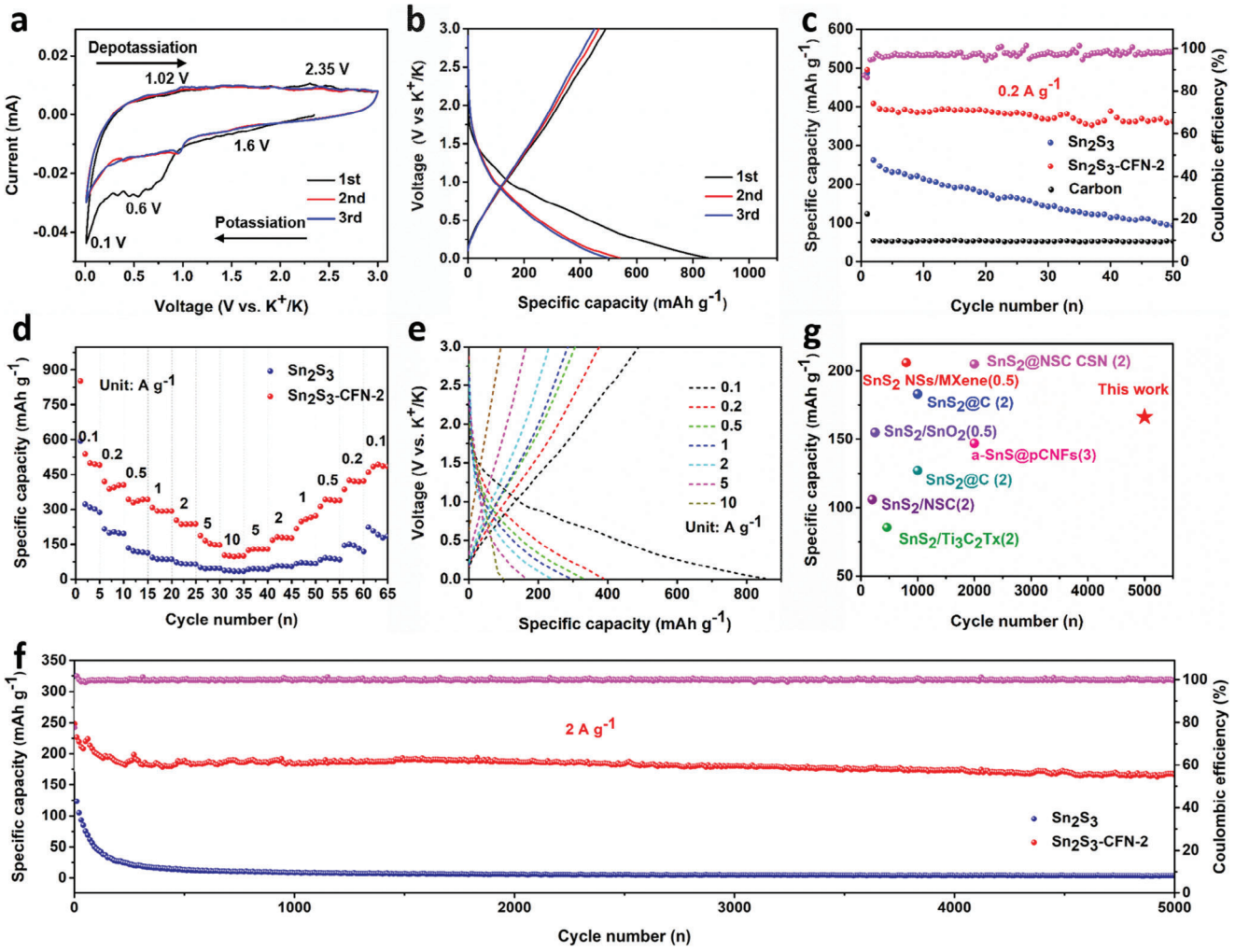

Figure 4. Electrochemical potassium storage performances of Sn_2S_3-CFN-2 and pure Sn_2S_3 anodes. a) CV curves of Sn_2S_3-CFN-2 at a scan rate of 0.1 mV s^{-1} in a potential range of 0.01–3.0 V. b) GDC profiles of Sn_2S_3-CFN-2 at a current density of 0.1 A g^{-1}. c) Cycling performance of Sn_2S_3-CFN, bulk Sn_2S_3 and carbon electrodes at a current density of 0.2 A g^{-1}. d) Rate performance of Sn_2S_3-CFN-2 and bulk Sn_2S_3 electrodes with current densities ranging from 0.1 to 10 A g^{-1}. e) Charge and discharge profiles at current densities ranging from 0.1 to 10 A g^{-1}. f) Cycling performance of Sn_2S_3-CFN-2 and bulk Sn_2S_3 electrodes at a current density of 2 A g^{-1}. g) Comparison of cycling performance between Sn_2S_3-CFN-2 and other representative Sn-S-based anodes for PIBs. h) CV curves of Sn_2S_3-CFN-2 under various sweep rates from 0.1 to 0.9 mV s^{-1}. i) *b* values calculated according to the slope of fitted log(*i*) against log(*v*) plots. j) The capacitive contribution ratio at different scan rates for Sn_2S_3-CFN-2.

0.45% per cycle, indicating its superior electrochemical cycle stability. To understand the superior electrochemical properties of Sn_2S_3-CFN-2 nanocomposites, the electrode morphology after 300th charge/discharge cycles at the current of 2.0 A g^{-1} was characterized by SEM and TEM (Figures S8 and S9, Supporting Information). The structure of Sn_2S_3-CFN-2 can still retain the original morphology upon repeated potassium insertion/extraction, demonstrating good structural stability and cycling performance. While the pure Sn_2S_3 particles without carbon modification suffered from serious pulverization and aggregation after 300 cycles at 2.0 A g^{-1} (Figure S10, Supporting Information). For the Sn_2S_3-CFN-2 anode, the outstanding cycling retention was mainly attributed to its 3D network structure for the accommodation of volume variation, as well as abundant active sites and Sn_2S_3 QDs for highly efficient electron and ion transport during cycles, thus giving rise to superior cycling stability with high capacities. Such electrochemical performance in PIBs is one of the best results for tin sulfide-based anodes in the literature (Figure 4g).[25]

In order to gain deeper insights into the exceptional rate performance of the Sn_2S_3-CFN-2 electrode in SIBs, we performed a kinetic reaction analysis by measuring CV curves at various scan rates ranging from 0.1 to 0.9 mV s^{-1} (Figures S11 and S12, Supporting Information). The CV curves obtained from the Sn_2S_3-CFN-2 electrode demonstrate excellent reversibility and a negligible degree of polarization, with similar shapes and slight peak shifts. However, at higher scan rates, the anodic peak shifts slightly to a positive potential, while the cathodic peak shifts to a negative potential, which is attributed to increased polarization in the electrode under these conditions. Generally, the peak current (*i*) and sweep rate (*v*) obey the following equation:[26]

$$i = av^b \quad (1)$$

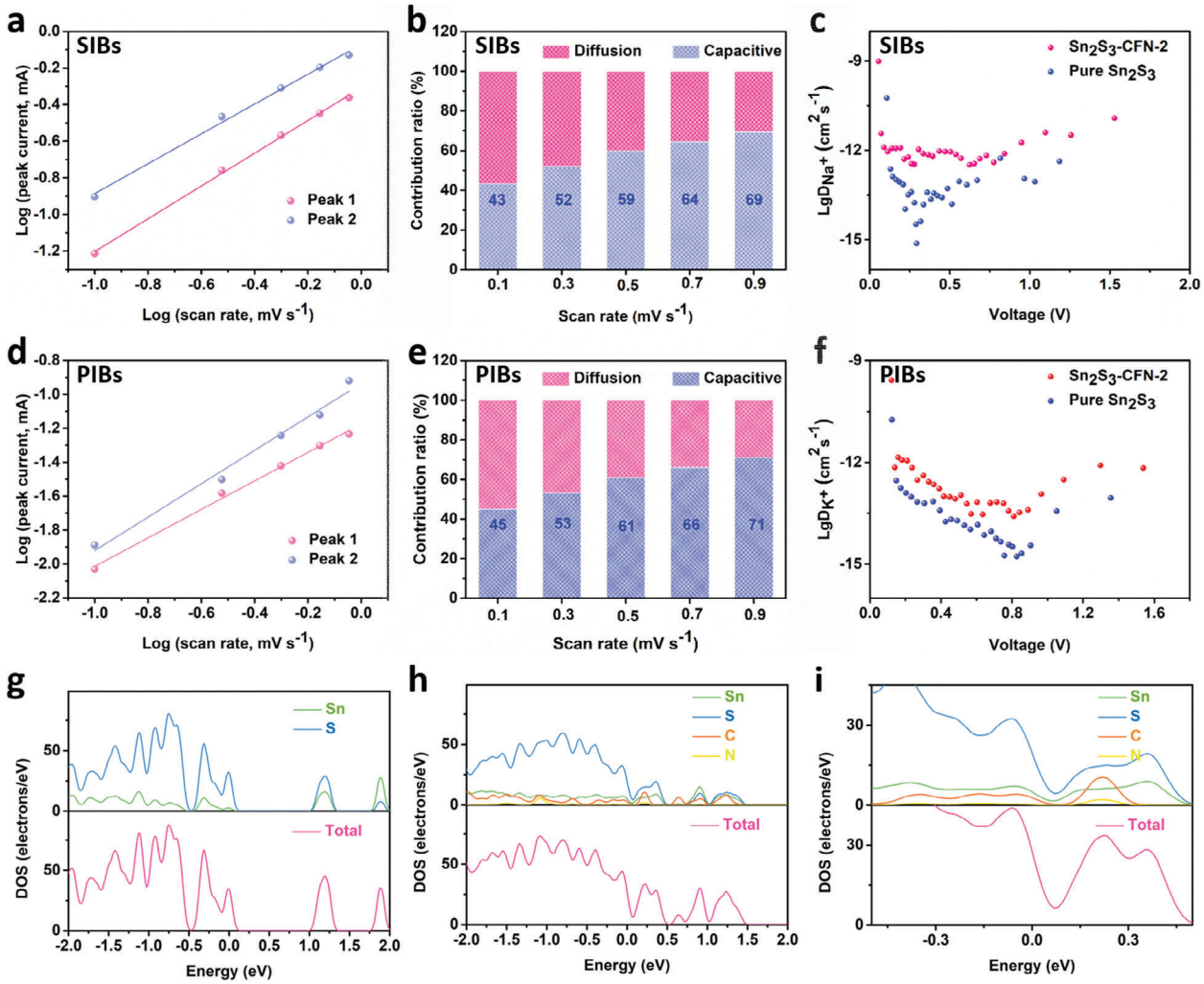

Figure 5. a,d) b values calculated in SIBs and PIBs according to the slope of fitted log(i) against log(v) plots. b,e) The capacitive contribution ratio in SIBs and PIBs at different scan rates for the Sn_2S_3-CFN-2 composite. c,f) The variation of Na^+ and K^+ diffusion coefficients with the voltage at the first discharge process. g–i) DOS of Sn_2S_3 and Sn_2S_3-CFN-2.

$$\log(i) = b\log(v) + \log(a) \quad (2)$$

where a and b are parameters. Note that the b value can be calculated from the slope of the curves of Equation (2) by plotting the logarithm of the peak current (log (i)) versus the logarithm of the scan rate (log (v)). The Na^+/K^+ storage mechanism can be determined by the value of b:b = 0.5 suggests that the charge/discharge process is controlled by the diffusion mechanism, while b = 1.0 indicates a pseudo-capacitive behavior.[27] The calculated b values ((**Figure 5a**) are approximately 0.89 (peak 1) and 0.81 (peak 2), indicating the prominent contribution of Faradaic pseudo-capacitance in the kinetics of each peak concomitant with a diffusion-controlled mechanism. The calculated b-values in PIBs of peak 1 and peak 2 (Figure 5d) were 0.84 and 0.98, respectively. Moreover, the capacitive contribution can be quantitatively calculated using the following equation:[28]

$$i(v) = k_1 v + k_2 v^{1/2} \quad (3)$$

where k_1 and k_2 are adjustable values, and $k_1 v$ and $k_2 v^{1/2}$ are the pseudo-capacitance-controlled and diffusion-controlled, respectively. The contribution of capacitive behavior in SIBs increases significantly from 43% to 69% as the scan rate is increased from 0.1 to 0.9 mV s^{-1}, leading to an improvement in capacity and rate performance (Figure 5b). The contribution ratios of capacitive behavior in PIBs for the Sn_2S_3-CFN-2 electrode also increase with an increase in scan rate. At scan rates of 0.1, 0.3, 0.5, 0.7, and 0.9 mV s^{-1}, the capacitive contributions are 45%, 53%, 61%, 66%, and 71%, respectively (Figure 5e). This gradual increase in capacitive behavior demonstrates the electrode's ability to maintain its high performance at higher scan rates. Figures S13 and S14, Supporting Information, illustrate examples of the separated pseudo-capacitive contribution in SIBs and PIBs of the Sn_2S_3-CFN-C electrode at a scan rate of 0.5 mV s^{-1}, with pseudo-capacitive contributions of 59% and 61%, respectively. The high percentage of the capacitive contribution from the mixed behaviors suggests that pseudo-capacitance plays a crucial role in the Na/K ion storage.

To further understand the improved electrochemical performance of Sn_2S_3-CFN-2, Na^+/K^+ diffusion coefficient in different stages of the first discharge process and conductivity properties were evaluated by galvanostatic intermittent titration (GITT) and density of states (DOS). The Na/K ion diffusion coefficient of Sn_2S_3-CFN-2 was determined by the following equation:[29]

$$D^{\mathrm{GITT}} = \frac{4}{\pi\tau}\left(\frac{m_B V_M}{M_B S}\right)^2\left(\frac{\Delta E_S}{\Delta E_t}\right)^2 \quad (4)$$

The equation involves various parameters, such as the relaxation time (τ), the mass of the active materials (m_B), molar mass (M_B), molar volume (V_M), geometric area of the electrode (S), voltage change caused by a pulse (ΔE_t), and constant current charging/discharging (ΔE_s). The sodium and potassium diffusion coefficients at the first discharge states were evaluated and compared with those of bulk Sn_2S_3. As shown in Figure 5c and Figure S15, Supporting Information, the sodium-ion diffusion coefficient of Sn_2S_3-CFN-2 is on the order of 10^{-12} cm^2 s^{-1} during the sodiation process. While undergoing sodiation, the sodium-ion diffusion coefficient gradually decreases until it reaches a demarcation point at around 0.8 V. However, as the cell voltage drops to approximately 0.1 V, there is a sudden and notable increase in the sodium-ion diffusion coefficient, indicating a novel electrochemical phenomenon—sodium metal-nanovoids filling at this particular point.[30] In contrast, the pure Sn_2S_3 displays an inferior diffusion coefficient. In comparison to the pure Sn_2S_3 system, the incorporation of a carbon nanofiber network into the Sn_2S_3 quantum dots system seems to mitigate the significant decrease in the diffusion coefficient of Na^+ around 0.25 V. This effect can be attributed to enhanced conductivity, facilitated electron transport, mitigation of structural changes, and the establishment of a conductive network facilitated by the carbon nanofibers and Sn_2S_3 quantum dots. The potassium diffusion coefficients of Sn_2S_3-CFN-2 are also higher than those of bulk Sn_2S_3. The plateau region of discharge profiles showed the lowest Na/K ion diffusion coefficient, indicating sluggish electrochemical reactions due to the high kinetic barriers associated with the simultaneous insertion of Na/K ion and structural development. The higher ionic conductivity observed in the presence of carbon modification, when compared to Sn_2S_3, is the primary contributing factor. Additionally, the porous carbon fiber network framework creates channels that facilitate the permeation of electrolytes and enhance sodium ion accessibility. To investigate the effect of N, S co-doped carbon on the conductivity of Sn_2S_3, DOS calculation was performed. As seen from Figure 5g, the pure Sn_2S_3 exhibits certain metallic conductivity properties with a bandgap of 0.775 eV. After integration with N, S co-doped carbon, the Sn_2S_3-CFN-2 composite become conductive, and a downward shift in the conduction band was observed (Figure 5h). The DOS distribution of N, S co-doped C/Sn_2S_3 reveals that C, N, and S atoms introduce additional energy levels into the Sn_2S_3 matrix, resulting in changes in the electronic properties of the material. Specifically, they introduce new energy states near the Fermi level, which can increase the density of states in the conduction band and thus enhance the material's electrical conductivity (Figure 5i). These DOS results reveal that the addition of a carbon layer and S, N co-doping can significantly enhance the electrical conductivity of Sn_2S_3 anodes, offering more possibilities for charge transfer and leading to the improvement of sodium storage capacity.

To delve deeper into the Na/K ion storage mechanism of Sn_2S_3, ex situ XRD was employed in conjunction with ex situ TEM to characterize the potential phases at various charge–discharge states. First, focusing on the Na ion storage mechanism, the XRD and TEM characterizations are presented in Figure S16, Supporting Information). In Figure S16a, Supporting Information, upon discharging to 0.01 V, the distinctive peaks associated with Sn_2S_3 completely vanish. Instead, characteristic peaks of metallic Sn (JCPDS no. 65-7657) emerge at 30.6°, 31.9°, and 44.9°. Simultaneously, two peaks at 31.9° and 33.3° appear, corresponding to $Na_{15}Sn_4$ (JCPDS no. 65-2166), affirming the formation of Sn and $Na_{15}Sn_4$ and the involvement of a conversion reaction during sodium ion storage. Upon charging the cell to 3 V, the weak peaks of Sn_2S_3 are observed, indicating the reversible conversion and alloying reactions of Sn_2S_3, thereby suggesting the amorphization of Sn_2S_3 following sodium ion extraction. Furthermore, the characteristic peak of Sn weakens, suggesting the presence of trace amounts of metallic Sn remaining after charging to 3 V. Ex situ HRTEM measurements was used to further verify the above phase transformation. At discharged to 0.01 V, the lattice spacing of 0.468 nm can be indexed to the (220) plane of $Na_{15}Sn_4$, and the lattice fringe of 0.278 nm corresponds well with the (1 0 1) facet of metallic Sn (Figure S16b, Supporting Information). When charged to 3 V, the distinct lattice spacing observed in Figure S16c, Supporting Information, can be attributed to the (222) crystallographic plane of Sn_2S_3 with interlayer distances of 0.332 nm. Simultaneously, the lattice fringe of 0.279 nm corresponds to the (101) facet of metallic Sn.

Secondly, in order to further investigate the K ion storage mechanism, ex situ XRD was also measured to characterize the possible phases at fully discharge state (0.01 V) and fully discharge state (3 V). As shown in Figure S17a, Supporting Information. When discharged to 0.01 V, the distinctive peaks associated with Sn_2S_3 vanish completely. Meanwhile, characteristic peaks of metallic Sn (JCPDS no. 65-7657) are evident at 30.6°, 31.9°, and 44.9°. At the same time, a peak emerges at 31.0°, identified as K_2S_6 (JCPDS no. 31-1096). another peak at 43.8° appear, corresponding to K_4Sn_{13} (JCPDS no. 65-3351). After charging the cell to 3 V, faint peaks of Sn_2S_3 become apparent, signifying the reversible conversion and alloying reactions of Sn_2S_3. This observation implies the amorphization of Sn_2S_3 following the extraction of potassium ions. Additionally, the distinctive peak of Sn diminishes, indicating the existence of trace amounts of metallic Sn that persist after charging to 3 V. Ex situ HRTEM measurements were applied to further confirm the mentioned phase transformation. Upon discharging to 0.01 V, the interlayer distances of 0.528 and 0.279 nm remain consistent with the (111) and (101) crystallographic planes of K_2S_6 and Sn, respectively (Figure S17b, Supporting Information). Notably, the lattice spacing of 0.351 nm is attributed to the (222) plane of K_4Sn_{23}. Upon charging to 3 V, the distinct lattice spacing depicted in Figure S17c, Supporting Information, is associated with the (222) crystallographic plane of Sn_2S_3, featuring interlayer distances of 0.332 nm. This observation clearly illustrates the reversibility of Sn_2S_3-CFN-2 composites in electrochemical reactions. Simultaneously, the lattice fringe of 0.279 nm corresponds to the (1 0 1) facet of metallic Sn.

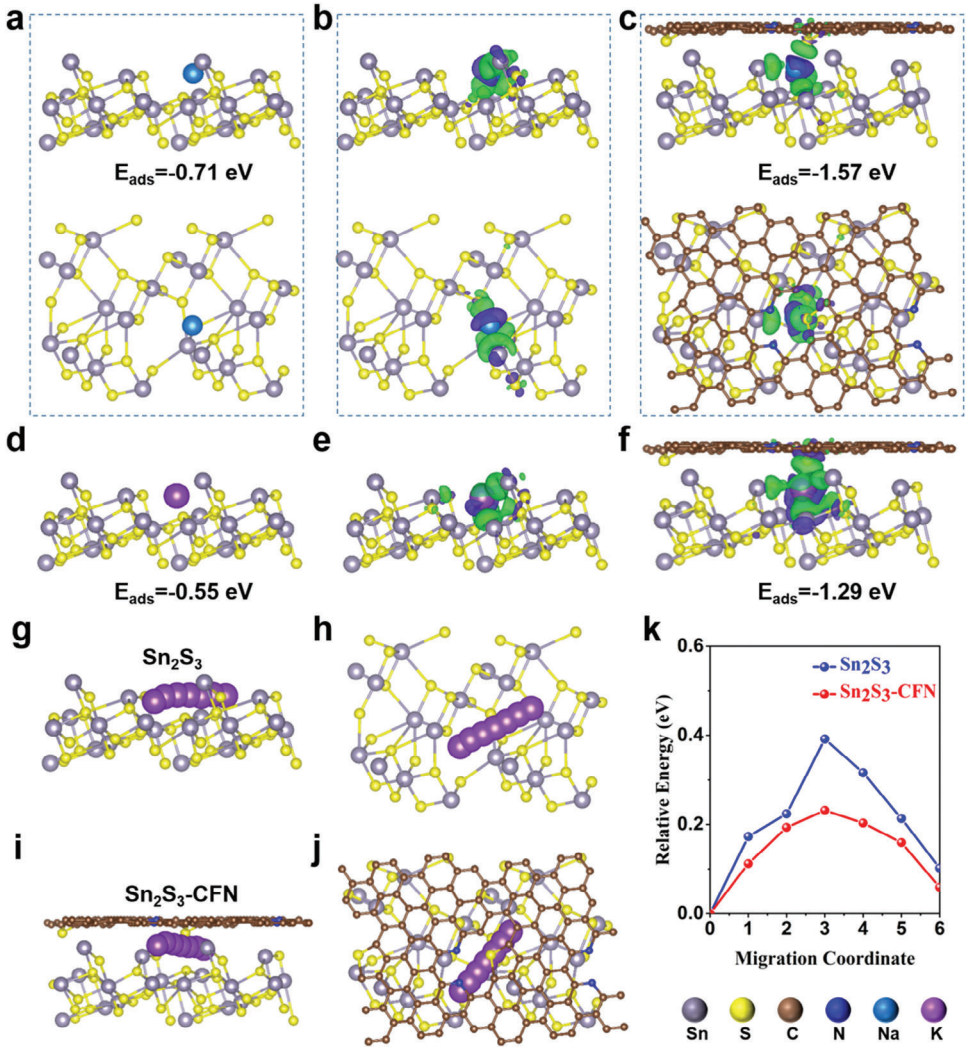

Figure 6. a) The first-principles calculation models with one Na atom adsorbed on Sn_2S_3 (side view and top view). b,c) Charge density differences with one Na atom adsorbed for Sn_2S_3 and Sn_2S_3-CFN (side view and top view). d) Calculation models with one K atom adsorbed on Sn_2S_3. e) and f) Charge density differences with one K atom adsorbed for Sn_2S_3 and Sn_2S_3-CFN. For charge density differences, green and blue areas represent the charge accumulation and loss, respectively. In addition, the corresponding adsorption energy is marked under the model. g,i) Side and h,j) top views of the K atom migration path and k) K atom diffusion energy barrier on g,h) the Sn_2S_3 surface and i,j) Sn_2S_3-CFN heterointerface, disclosing the lower diffusion barrier in the Sn_2S_3-CFN interface than that of the Sn_2S_3 surface.

To further elucidate the influence of the N, S co-doped carbon matrix on the ion storage/diffusion capacity of Sn_2S_3-CFN composites, we conducted adsorption energy and ion migration calculations. The adsorption energies (E_{ads}) were first utilized to analyze the energy variations. As illustrated in **Figure** 6a,c,d,f, the E_{ads} values between the Na/K atom and the (111) surface of Sn_2S_3 or the interface of Sn_2S_3 and N, S co-doped carbon were determined to be −0.63 eV/−1.57 eV and −0.55 eV/−1.29 eV, respectively, indicating stronger interactions between the Na/K atom and Sn_2S_3-CFN. Figure 6b,c exhibits the charge density differences with one Na atom adsorbed for Sn_2S_3 and Sn_2S_3-CFN systems, respectively. The green and blue regions represent charge accumulation and depletion, respectively, revealing the transfer of charge from the Na atom to the samples. In the Sn_2S_3-CFN-2 system, the charge accumulation happened not only between the Na atom and Sn_2S_3 but also between the Na atom and N, S co-doped carbon layer. Notably, the charge accumulation region around Sn_2S_3-CFN heterointerface is larger than that of the pure Sn_2S_3 surface, suggesting a strong binding energy between the Na atom and Sn_2S_3-CFN, which is consistent with the E_{ad} calculation. Additionally, the charge accumulated around N and S atoms in the carbon layer was observed, indicating partial charge transfer from Na to N and S atoms. A similar charge transfer and accumulation phenomenon was observed between K atom and Sn_2S_3 and Sn_2S_3-CFN systems (Figure 6e,f, and Figure S18, Supporting Information). These results demonstrate that the N, S co-doped carbon coating can enhance the Na/K atom adsorption ability of Sn_2S_3-CFN, thereby enhancing the ion storage capacity. Furthermore, another vital factor that determines the suitability of anode materials for practical applications is the mobility of adsorbed atoms on the Sn_2S_3 surface, which is closely related to cycling performance. Since there has been no previous research

on the diffusion of K atoms in the Sn_2S_3 system, and Sn_2S_3-CFN exhibits a similar ion storage mechanism in both SIBs and PIBs, it is important to investigate the diffusion energy barriers of K atoms to assess the potential of Sn_2S_3-CFN as an anode material for both battery systems. The K-ion migration paths are illustrated in Figure 6g,h for the Sn_2S_3 surface and Figure 6i,j for the Sn_2S_3-CFN system. The diffusion energy barriers for Sn_2S_3-CFN were much lower than those for Sn_2S_3, indicating that the N, S co-doped carbon layer can facilitate the K-ion diffusion kinetics. The results of these calculations indicate that the addition of a carbon layer can significantly improve the ion transport/adsorption ability of Sn_2S_3 anode material. Consequently, Sn_2S_3-CFN anodes display greatly enhanced electrochemical performance compared to pure Sn_2S_3 anodes.

3. Conclusion

In summary, Sn_2S_3 QDs with a size of approximately 1.6 nm embedded in N, S co-doped carbon fiber networks were successfully synthesized involving sequential steps of freeze-drying, carbonization, and sulfidation. The Sn_2S_3 QDs can shorten the ion diffusion distance, buffer the volume change, and facilitate the overcoming of the kinetic and thermodynamic barriers of electrochemical reactions. In addition, the N, S co-doped carbon fiber network structure exhibits the ability to accommodate volume change, offer more reversible active sites for sodium/potassium ions storage, and enhance electrical conductivity. Experimental results and DFT calculations indicated that the N, S co-doped carbon modification prevented Sn_2S_3 QD aggregation and growth, while also reducing both the adsorbed energies and diffusion energy barriers of Na/K atoms in the interlayer of Sn_2S_3-CFN, thereby enhancing the reactivity of the material for sodium/potassium storage. As a result, the Sn_2S_3-CFN composite exhibited excellent battery performance. As anode materials, it displayed high reversible capacities and excellent rate capability (250.0 mAh g^{-1} at 20 A g^{-1} for SIBs and 100.0 mAh g^{-1} at 10 A g^{-1} for PIBs), as well as superior long-term cycling stability (279.6 mAh g^{-1} after 10 000 cycles at 5 A g^{-1} for SIBs and 166.3 mAh g^{-1} after 5 000 cycles at 2 A g^{-1} for PIBs). This work may pave the way for the design and fabrication of high-performance electrode materials for SIBs and PIBs, with potential applications extending to other rechargeable battery systems.

4. Experimental Section

Chemical: The raw materials of tin (II) chloride dihydrate ($SnCl_2 \cdot 2H_2O$, ACS reagent, 98%), chitosan ($(C_6H_{11}NO_4)_n$, medium molecular weight), tin sulfide (Sn_2S_3, 99.95%), and sulfur (S, 99.99%) were purchased and used without further purification.

Material Synthesis: In a typical synthesis, 0.33 g of chitosan powder was completely dissolved in 100 mL acetic acid solution. Subsequently, 5 mL of 0.886 M $SnCl_2{\cdot}2H_2O$ solution was added dropwise into the chitosan solution with stirring. The solution was allowed to be stirred for another 1 h to ensure the formation of a homogeneous solution. The mixture solution was rapidly frozen and subsequently freeze-dried to remove water at −50 °C for 72 h. The as-prepared Sn-chitosan precursors were then heated to 600 °C for 4 h with a heating rate of 2 °C min^{-1} under Ar flow. Subsequently, the pretreated samples were further sulfurized in a tube furnace (in a weight ratio of 1:2) and heated to 450 °C in Ar flow (2 °C min^{-1}) and kept at 450 °C for 3 h, yielding 3D architecture Sn_2S_3/C composite (denated as Sn_2S_3-CFN-2). For comparison, Sn_2S_3-CFN-1 and Sn_2S_3-CFN-3 were fabricated under the similar preparation procedures, differing only in the amount of chitosan used as precursors—0.165 g for Sn_2S_3-CFN-1 and 0.66 g for Sn_2S_3-CFN-3, respectively. Furthermore, carbon materials doped solely with N and S (referred to as Carbon) were also prepared using the same procedure, omitting the inclusion of a Sn source.

Materials Characterization: The material phases were analyzed by X-ray diffraction (XRD, Rigaku D/max 2000 diffractometer) operating at Cu Kα radiation. The microstructure and morphology of the samples were investigated by a field-emission scanning electron microscope (FE-SEM-4800-1, Japan) and transmission electron microscopy (TEM, Thermo Fischer Talos F200x) coupled with an EDX spectrometer. The element chemical states were analyzed by X-ray photoelectron spectroscopy (XPS, Thermo Scientific K-Alpha$^+$). Raman spectra were recorded by an Xplora Raman spectrometer (Xplora, France).

Electrochemical Measurements: In this study, the sodium- and potassium-ion storage properties of Sn_2S_3-CFN composites and pure Sn_2S_3 were investigated. To prepare the working electrodes, a mixture of active materials, acetylene black, and binder carboxymethyl cellulose (CMC) (in a weight ratio of 7:2:1) was homogeneously dispersed in water and coated onto a copper foil, which was then vacuum dried at 80 °C for 12 h. The mass loading per electrode was approximately 0.7−1.0 mg cm^{-2}. The CR2032 coin cells were assembled in an argon-filled glove box, with sodium metal and potassium metal used as counter electrodes for SIBs and PIBs, respectively. Glass fiber paper was used as the separator. The electrolyte for SIBs was composed of 1 M $NaClO_4$ dissolved in ethylene carbonate (EC) and diethyl carbonate (DEC) (in a 1:1 volume ratio) with 10 wt% fluoroethylene, while the electrolyte for PIBs was 0.8 M KPF_6 dissolved in EC/DEC (in a 1:1 volume ratio). The galvanostatic discharge/charge (GDC) tests of SIBs and PIBs were conducted on the NETWARE BTS-5 V battery test system, with voltage ranges of 0.01–3.0 V. Cyclic voltammetry (CV) curves were measured using a CHI 660D electrochemical workstation.

First-Principles Calculations: The Perdew-Burke-Ernzerhof (PBE) formulation within the generalized gradient approximation (GGA) was employed for DFT calculations.[31] The interactions between valence electrons and ionic cores were described using the projector augmented wave (PAW) method.[32] Partial occupancies of the Kohn–Sham orbitals were allowed using the Gaussian smearing method, with a width of 0.05 eV. The electronic energy was considered self-consistent when the energy change was less than 10^{-5} eV, while the geometry optimization was considered convergent when the energy change was less than 0.03 eV $Å^{-1}$. T An energy cutoff of 450 eV was set, and 2 × 2 × 1 Monkhorst-Pack k-point sampling was performed for Brillouin zone integration of the structure. The adsorption energies (E_{ads}) were calculated as $E_{ads} = E_{ad/sub} - E_{ad} - E_{sub}$, where $E_{ad/sub}$, E_{ad}, and E_{sub} are the total energies of the optimized adsorbate/substrate system, the adsorbate in the structure, and the clean substrate, respectively. The Climbing Image-Nudged Elastic Band methods had been employed to calculate the K ions migration barriers in the structures.

Supporting Information

Supporting Information is available from the Wiley Online Library or from the author.

Acknowledgements

This work was supported by National Natural Science Foundation of China (51971065), and the Innovation Program of Shanghai Municipal Education Commission (2019-01-07-00-07-E00028). The authors thank SCI-GO (www.sci-go.com) for the TEM analysis.

Conflict of Interest

The authors declare no conflict of interest.

Data Availability Statement

The data that support the findings of this study are available in the supplementary material of this article.

Keywords

N, S co-doped carbon fiber network, potassium-ion battery, Sn_2S_3 quantum dot, sodium-ion battery, theoretical calculation

Received: December 2, 2023
Published online:

[1] a) K. R. Abbasi, M. Shahbaz, J. Zhang, M. Irfan, R. Alvarado, *Renewable Energy Rev.* **2022**, *187*, 390; b) I. Hanif, *Energy Strategy Rev.* **2018**, *21*, 16; c) M. Murshed, Z. Ahmed, M. S. Alam, H. Mahmood, A. Rehman, V. Dagar, *Environ. Sci. Pollut. Res.* **2021**, *28*, 67689; d) H. C. Hesse, M. Schimpe, D. Kucevic, A. Jossen, *Energies* **2017**, *10*, 2107; e) M. Li, J. Lu, Z. Chen, K. Amine, *Adv. Mater.* **2018**, *30*, 1800561; f) L. B. Diaz, X. He, Z. Hu, F. Restuccia, M. Marinescu, J. V. Barreras, Y. Patel, G. Offer, G. Rein, *J. Electrochem. Soc.* **2020**, *167*, 090559.

[2] a) H. Wu, G. Xia, X. Yu, *EnergyChem* **2023**, *5*, 100095; b) H. Wu, Z. Xiong, Y. Mao, H. Zhang, Y. Hu, J. Shen, B. Wang, X. Yu, *J. Mater. Sci. Technol.* **2023**, *143*, 43; c) P. Du, L. Cao, B. Zhang, C. Wang, Z. Xiao, J. Zhang, D. Wang, X. Ou, *Renewable Sustainable Energy Rev.* **2021**, *151*, 111640.

[3] Y. Xie, Y. Dall'Agnese, M. Naguib, Y. Gogotsi, M. W. Barsoum, H. L. Zhuang, P. R. Kent, *ACS Nano* **2014**, *8*, 9606.

[4] a) E. Wang, M. Chen, X. Guo, S. L. Chou, B. Zhong, S. X. Dou, *Small Methods* **2020**, *4*, 1900163; b) C. Zhang, H. Zhao, Y. Lei, *Energy Environ. Mater.* **2020**, *3*, 105; c) M. Lao, Y. Zhang, W. Luo, Q. Yan, W. Sun, S. X. Dou, *Adv. Mater.* **2017**, *29*, 1700622; d) K. Song, C. Liu, L. Mi, S. Chou, W. Chen, C. Shen, *Small* **2021**, *17*, 1903194; e) T. Wu, W. Zhang, J. Yang, Q. Lu, J. Peng, M. Zheng, F. Xu, Y. Liu, Y. Liang, *Carbon Energy* **2021**, *3*, 554; f) B. Huang, Z. Pan, X. Su, L. An, *J. Power Sources* **2018**, *395*, 41; g) L. Li, Y. Zheng, S. Zhang, J. Yang, Z. Shao, Z. Guo, *Energy Environ. Sci.* **2018**, *11*, 2310; h) F. Zhang, J. Chen, J. Yang, *Adv. Fiber Mater.* **2022**, *4*, 720; i) H. Zhang, C. Wang, H. Luo, J. Chen, M. Kuang, J. Yang, *Angew. Chem.* **2023**, *135*, 202217071.

[5] Y. Zhang, B. Guo, L. Hu, Q. Xu, Y. Li, D. Liu, M. Xu, *J. Alloys Compd.* **2018**, *732*, 448.

[6] T. Zeng, G. Chen, Q. Peng, D. Feng, Q. Wang, *ChemSusChem* **2021**, *14*, 2383.

[7] H. Guan, D. Feng, T. Zeng, *Ceram. Int.* **2022**, *48*, 11074.

[8] a) G. Chen, X. Li, T. Zeng, R. Han, Q. Wang, *Carbon* **2021**, *171*, 464; b) C. Zhang, F. Wang, F. Qi, Y. Wang, S. Feng, J. Tan, Z. Xiang, J. Guo, S. He, C. Ye, *Energy Fuels* **2022**, *36*, 14423.

[9] Y. Wang, H. Li, S. Chen, B. Zhai, S. Di, G. Gao, S. Lee, S. Chun, S. Wang, L. Li, *Sci. Bull.* **2022**, *67*, 2085.

[10] Y. Jiang, M. Wei, J. Feng, Y. Ma, S. Xiong, *Energy Environ. Sci.* **2016**, *9*, 1430.

[11] a) Z. Zhang, R. Wang, J. Zeng, K. Shi, C. Zhu, X. Yan, *Adv. Funct. Mater.* **2021**, *31*, 2106047; b) Y. Liu, C. Yang, Q. Zhang, M. Liu, *Energy Storage Mater.* **2019**, *22*, 66.

[12] a) Q. Guo, Y. Ma, T. Chen, Q. Xia, M. Yang, H. Xia, Y. Yu, *ACS Nano* **2017**, *11*, 12658; b) X. Wang, Y. Liu, Y. Wang, L. Jiao, *Small* **2016**, *12*, 4865; c) W. Wei, Y. Zhang, L. Liang, K. Wang, Q. Zhou, Y. Zhou, H. Wang, *Mater. Chem. Front.* **2021**, *5*, 7778; d) D. Kong, C. Cheng, Y. Wang, Z. Huang, B. Liu, Y. Von Lim, Q. Ge, H. Y. Yang, *J. Mater. Chem. A* **2017**, *5*, 9122.

[13] L. Qian, H. Zhang, *Green Chem.* **2010**, *12*, 1207.

[14] X. Jiang, X. Yang, Y. Zhu, J. Shen, K. Fan, C. Li, *J. Power Sources* **2013**, *237*, 178.

[15] N. Shimodaira, A. Masui, *J. Appl. Phys.* **2002**, *92*, 902.

[16] I. Vlassiouk, S. Smirnov, I. Ivanov, P. F. Fulvio, S. Dai, H. Meyer, M. Chi, D. Hensley, P. Datskos, N. V. Lavrik, *Nanotechnology* **2011**, *22*, 275716.

[17] Z. Hu, X.-Y. Jiao, L. Xu, *Microchem. J.* **2020**, *154*, 104588.

[18] D. Avellaneda, I. Sánchez-Orozco, J. Martínez, S. Shaji, B. Krishnan, *Mater. Res. Express* **2018**, *6*, 016409.

[19] a) Z. Xu, Z. Zhang, L. Gao, H. Lin, L. Xue, Z. Zhou, J. Zhou, S. Zhuo, *RSC Adv.* **2018**, *8*, 40252; b) L. Ren, Z. Jin, S. Cai, J. Yang, Z. Hong, *Cryst. Res. Technol.* **2012**, *47*, 461.

[20] J. Li, X. Hou, Y. Mao, C. Lai, X. Yuan, *Energy Fuels* **2020**, *34*, 14995.

[21] J. Mei, J. Han, F. Wu, Q. Pan, F. Zheng, J. Jiang, Y. Huang, H. Wang, K. Liu, Q. Li, *Front. Chem.* **2022**, *10*, 1105997.

[22] L. Wan, P. Song, J. Liu, D. Chen, R. Xiao, Y. Zhang, J. Chen, M. Xie, C. Du, *J. Power Sources* **2019**, *438*, 227013.

[23] L. Xue, F. Chen, Z. Zhang, Y. Gao, D. Chen, *ChemElectroChem* **2022**, *9*, 202101327.

[24] a) Y. Wang, W. Kang, P. Ma, D. Cao, D. Cao, Z. Kang, D. Sun, *Mater. Chem. Front.* **2020**, *4*, 1212; b) H. Dong, X. Wang, J. Jiang, W. Lin, E. Liu, J. Kang, C. Shi, J. Sha, B. Chen, L. Ma, *Chem. Eng. J.* **2023**, *460*, 141827; c) Y. Sun, Y. L. Yang, X. L. Shi, L. Ye, Y. Hou, J. Wang, G. Suo, S. Lu, Z. G. Chen, *Battery Energy* **2023**, *2*, 20220046; d) J. Lin, L. Yao, C. Zhang, H. Ding, Yuanhui, Wu, S. Li, J. Han, G. Yue, D. Peng, *ACS Sustainable Chem. Eng.* **2021**, *9*, 11280; e) Y. Zhang, H. Su, C. Wang, D. Yang, Y. Li, W. Zhang, H. Wang, J. Zhang, D. Li, *Nanoscale* **2019**, *11*, 12846; f) L.-b. Tang, P.-y. Li, T. Peng, H.-X. Wei, Z. Wang, H.-y. Wang, C. Yan, J. Mao, K. Dai, X.-w. Wu, *J. Electroanal. Chem.* **2023**, *928*, 117077.

[25] a) J. Si, X. Liu, Z. Wang, S. Zhang, C. Deng, *J Energy Chem* **2023**, *76*, 349; b) D. Li, L. Dai, X. Ren, F. Ji, Q. Sun, Y. Zhang, L. Ci, *Energy Environ. Sci.* **2021**, *14*, 424; c) R. Li, J. Wu, J. He, X. Li, Y.-W. Mai, Y. Chen, X. Li, *Composites, Part B* **2022**, *243*, 110132; d) K. Cao, S. Wang, Y. Jia, D. Xu, H. Liu, K.-J. Huang, Q.-S. Jing, L. Jiao, *Chem. Eng. J.* **2021**, *406*, 126902; e) H. Liu, Y. He, H. Zhang, S. Wang, K. Cao, Y. Jiang, X. Liu, Q.-S. Jing, *J. Colloid Interface Sci.* **2022**, *606*, 167; f) Y. Cao, H. Chen, Y. Shen, M. Chen, Y. Zhang, L. Zhang, Q. Wang, S. Guo, H. Yang, *ACS Appl. Mater. Interfaces* **2021**, *13*, 17668.

[26] Z. Zhang, J. Liang, X. Zhang, W. Yang, X. Dong, Y. Jung, *Int. J. Hydrogen Energy* **2020**, *45*, 8186.

[27] D. Lin, K. Li, Q. Wang, L. Lyu, B. Li, L. Zhou, *J. Mater. Chem. A* **2019**, *7*, 19297.

[28] J. Zhang, H. Jiang, Y. Zeng, Y. Zhang, H. Guo, *J. Power Sources* **2019**, *439*, 227026.

[29] X. Rui, N. Ding, J. Liu, C. Li, C. Chen, *Electrochim. Acta* **2010**, *55*, 2384.

[30] S. Komaba, W. Murata, T. Ishikawa, N. Yabuuchi, T. Ozeki, T. Nakayama, A. Ogata, K. Gotoh, K. Fujiwara, *Adv. Funct. Mater.* **2011**, *21*, 3859.

[31] a) G. Kresse, J. Furthmüller, *Phys. Rev. B* **1996**, *54*, 11169; c) J. P. Perdew, K. Burke, M. Ernzerhof, *Phys. Rev. Lett.* **1996**, *77*, 3865; d) G. Kresse, J. Furthmüller, *Comput. Mater. Sci.* **1996**, *6*, 15.

[32] a) G. Kresse, D. Joubert, *Phys. Rev. B* **1999**, *59*, 1758; b) P. E. Blöchl, *Phys. Rev. B* **1994**, *50*, 17953.